Pergamon

Int. J. Impact Engng Vol. 19, No. 3, pp. 189–206, 1997

PII:S0734-743X(97)00028-0 0734-743X/97 $17.00 + 0.00

DYNAMIC DUCTILE RUPTURE UNDER CONDITIONS OF PLANE STRAIN

M. ZHOU* and R. J. CLIFTON†

* George W. Woodruff School of Mechanical Engineering, Georgia Institute of Technology, Atlanta, GA 30332–0405, U.S.A. and † Division of Engineering, Brown University, Providence, RI 02912, U.S.A.

(*Received* 20 *March* 1996; *in revised form* 7 *June* 1996)

Summary—A plate impact experiment is used to study dynamic ductile rupture at strain rates up to $10^5\,s^{-1}$ in a spheroidized 1045 steel. The material has a microstructure consisting of a fine dispersion of cementite particles embedded in ferrite particles. Plane strain tensile loading is generated by impacting a deeply notched specimen with a thin elastic flyer plate. The notch, parallel to the impact plane and extending halfway through the diameter, is filled with steel shims to transmit compressive stress waves. Upon reflection from the rear surface of the specimen, the waves become tensile in nature and cause an opening mode of loading at the blunt notch tip, resulting in ductile void nucleation and growth there. The nucleation of voids is observed to occur through particle–matrix debonding, particle fracture and particle–particle separation. Extensive void growth is observed at the notch tip as the impact velocity is increased. Relative notch opening displacement is found to depend on the initial notch width as well as the impact velocity. At impact velocities above 0.14 mm/μs, void nucleation due to the reflected tensile waves is also observed away from the notch along a plane parallel to the rear surface. This spallation is studied in one version of the plate impact experiment that does not involve a notch. Scanning electron microscopy of the rupture surfaces shows that spallation occurs mainly by cleavage of the ferrite grains and is assisted by void nucleation and growth on separate void sheets. Free surface velocities are monitored and analyzed at three points in front of the notch tip on the unnotched side by means of a normal velocity interferometer system. A dynamic finite element method based on a constitutive law proposed by Gurson for porous materials is used to simulate the experiments. The results have identified the mechanism for damage through the calculated and measured free surface velocity profiles. Copyright © 1997 Elsevier Science Ltd.

Keywords: ductile rupture, plate impact, spheroidized steel, 1045 steel, void growth.

NOTATION

f	particle volume fraction or void volume fraction
N_l	number of particles intersecting a line
L	test line length
d_s	mean particle diameter on a plane
d	mean particle diameter in 3D
λ	mean surface-to-surface distance between particles
$\dot{\bar{\varepsilon}}$	equivalent plastic strain rate
$\dot{\bar{\varepsilon}}_1, \dot{\bar{\varepsilon}}_2$	plastic strain rate functions
$\dot{\bar{\varepsilon}}_0, \dot{\bar{\varepsilon}}_m$	reference and limit plastic strain rates
a, m	rate sensitivity parameters
$g(\bar{\varepsilon})$	hardness function
$\bar{\varepsilon}$	equivalent plastic strain
$\bar{\sigma}$	equivalent stress
σ_0	reference stress
$\varepsilon_0, \varepsilon_r$	reference strains
ω, N	strain hardening parameters
σ_e	macroscopic equivalent stress
σ_h	macroscopic hydrostatic stress
σ, σ'	Cauchy and deviatoric Cauchy stress tensors
q_1, q_2	dilatancy and pressure sensitivity parameters
$\mathbf{D}^p$	plastic part of rate-of-deformation tensor
$\mathscr{D}, \mathscr{B}$	void nucleation functions
s_N	standard deviation for nucleation

1. INTRODUCTION

While second phase precipitates or particles greatly enhance the strength of materials by acting as obstacles to dislocation movement (see e.g. Dew-Hughes and Robertson [1], Meiklejohn and Skoda [2], Ashby [3], Kocks [4], Foreman and Makin [5], Liu and Gurland [6]), they also provide sites for the initiation of microvoids during plastic deformation. The nucleation, growth and subsequent coalescence of voids play the most important role in the process of ductile failure (Gurland and Plateau [7], Thomson and Hancock [8], and Thompson [9]). Voids nucleate through particle-matrix debonding and through particle cracking (Gurland and Plateau [7]). The early studies by McClintock [10] for a cylindrical void and Rice and Tracey [11] for a spherical void, focused on the quasistatic growth kinetics of a single cavity in an infinite elastic-plastic matrix. Their work showed the dependence of void growth on the triaxiality of the stress state. Brownrigg *et al.* [12] found that the superposition of pressure severely retards the nucleation and growth of voids at carbide particles and that fracture strain increases linearly with pressure in a spheroidized 1045 steel. Void initiation and growth are explained by Gurland and Plateau [7] and Broek [13] as a result of dislocation loop pile-ups against particles. The study by Park and Thompson [14] showed that void nucleation appears to be controlled by a stress-based criterion and that void growth and coalescence are controlled predominantly by plastic strain in tensile tests. Fisher and Gurland [15] found that larger particles and grain boundaries are more favorable sites for void nucleation.

There have been extensive studies of the ductile rupture process based on the continuum theory of plasticity. Berg [16] described the motion of an elliptical cavity in a plane viscous body by a conformal transformation. The deformation conditions under which an isolated void may become ellipsoidal and collapse into the shape of a crack or needle were studied by Budiansky *et al.* [17] and Budiansky [18]. Based on the hypothesis that coalescence is the result of internal necking of adjacent cavities, Thomason [19] analysed the evolution of a regular array of cavities subjected to plane strain triaxial stress states. Blume [20] studied the interaction between two contiguous spherical voids under radially symmetric remote loading in a hyperelastic solid and found that the voids are attracted to each other for most remote load triaxialities; separation is predicted only under stress states which are nearly uniaxial along the line of centers of the voids. The interactions between periodically distributed voids and their growth and collapse have also been analyzed by Nemat-Nasser and Iwakuma [21] and Nemat-Nasser, Iwakuma and Accorsi [22].

Gurson [23, 24] developed a phenomenological constitutive relation by introducing a plastic potential which depends on material strength, void volume fraction and hydrostatic stress. The effects of voids are represented by a single parameter, the void volume fraction, through which materials with any porosity exhibit macroscopic dilatancy and pressure sensitivity. Tvergaard [25, 26] modified the Gurson model by amplifying the void volume fraction and hydrostatic stress in order to bring predictions closer to the results of full numerical analyses at small void volume fractions. Tvergaard and Needleman [27] further modified the yield condition to model the loss of macroscopic stress-carrying capacity associated with void coalescence.

Several investigators have considered the effects of crystalline slip on the deformation of voids. Nemat-Nasser and Hori [28, 29, 30] showed that, as a result of the local anisotropic plastic flow by slip on crystallographic planes, an initially circular (2D) or spherical (3D) void quickly deforms into a noncircular (2D) or nonspherical (3D) shape even under all-around uniform tension or compression.

Hori and Nemat-Nasser [29, 30] studied the dynamic response of crystalline solids with micro-cavities based on an approximate method for calculating void deformation in crystalline bodies. They found that the global response of the material becomes tougher as loading rate is increased. Studies on void nucleation, growth and coalescence under dynamic conditions are reviewed by Curran, Seaman and Shockey [31]. One of the experimental configurations used to study ductile rupture under dynamic conditions involves impacting a flyer plate against a target specimen of the same or different material. Upon reflection from

the rear surface of the target the compressive wave becomes a tensile wave propagating in the opposite direction. This tensile wave causes initiation, growth and coalescence of voids, leading to spallation. Thorough reviews of spallation have been reported by Meyers and Aimone [32] and Asay and Kerley [33]. Continuum mechanics modeling of spallation based on void nucleation and growth has been done by Rajendran [34] and Eftis *et al.* [35] with finite difference methods.

The objective of the current study is to obtain dynamic rupture at strain rates up to $10^5\ s^{-1}$ caused by the non-uniform stress and strain fields resulting from the diffraction of a tensile stress wave by a pre-cut notch in the middle of a specimen in a plate impact configuration. One version of the experiment involves the use of a specimen without a notch. This type of specimen allows the damages caused by a plane tensile wave to be studied independently of the effects of the notch. In addition to the experiments, finite element simulations are carried out for the experiments. The simulations account for the initiation and growth of voids by using the modified Gurson model, Tvergaard [25,26]. This model is used to help us in identifying the damage mechanisms in the material studied. It is also used to interpret the damage signals in recorded surface velocity profiles from the experiments. This investigation does not involve a direct simulation of the ductile fracture process. Instead, the focus is on the damage process of void initiation and growth.

2. MATERIAL AND MATERIAL RESPONSE CHARACTERIZATION

The material is 1045 steel obtained in the form of cold drawn bars 2.5 inches in diameter. Its chemical composition is given in Table 1. The spheroidizing treatment involves austenitizing at 900°C for one hour, quenching in agitated ice water and normalizing at 700°C for (A) 24 hours, (B) 48 hours and (C) 120 hours. To obtain a fully martensitic structure required for achieving a uniform distribution of carbide spheroids during normalization, the material is cut into circular disks 62.5 mm in diameter and 10 mm in thickness to ensure a sufficiently high cooling rate. After normalization, the specimens are air-cooled to room temperature. Figures 1(a–c) show the microstructures produced by normalizations A, B and C, respectively. The microstructures are that of a spehroidized steel consisting of a fine dispersion of cementite particles embedded in a ferrite matrix. The particle size distributions are measured by an interception-line method which involves recording the number of particles intercepted by randomly placed test lines and the corresponding intercept lengths, for a plane section of

Table 1. Chemical composition of the 1045 steel, wt%

Fe	C	S	Mn	P
98.74	0.47	0.028	0.75	0.012

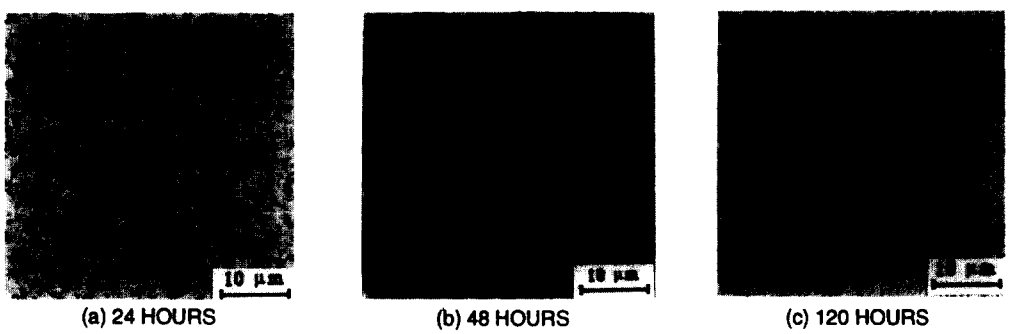

Fig. 1. Microstructures of spheriodized 1045 steel; (a) 24 hour normalization, (b) 48 hour normalization, and (c) 120 hour normalization.

Table 2. Microstructural parameters

Heat treatment	f %	d μm	σ_n μm	λ μm
A	6.54	0.54	0.43	5.14
B	6.52	0.84	0.75	8.03
C	6.58	1.18	0.90	11.17

the specimen. The particle volume fraction f is obtained by dividing the number of grid points falling in areas occupied by the particles by the total number of grid points in the area covered by a uniform test grid. The microstructural parameters obtained are listed in Table 2. These parameters obey the relations

$$f = N_l \cdot L = N_l \cdot \sqrt{\frac{2}{3}} d_s = N_l \cdot \frac{2}{3} d, \tag{1}$$

which are exact for uniform particles spherical in shape and randomly distributed (Ashby [3] and Underwood [36]). In Eqn (1), N_l is the number of intersections with the particles per unit test line, L is the mean particle intercept length, d_s is the mean particle diameter on a random section and d is the three-dimensional particle diameter. Also in Table 2, σ_n denotes the standard deviation of the particle diameter d, λ is the mean surface-to-surface particle distance calculated from $\lambda = L(1-f)/f$.

Pressure–shear plate impact experiments, as described by Clifton and Klopp [37], were conducted to study the material response under high strain rates on the order of $10^5\ s^{-1}$. The resulting dynamic stress–strain curves are shown in Fig. 2 together with those obtained at a lower strain rate of $4.05 \times 10^3\ s^{-1}$ with torsional Kolsky bar experiments and with quasistatic torsion experiments by Walter and Duffy [38] for a spheroidized 1045 steel with a microstructure similar to that produced by normalization C above. Clearly, the materials show a strong strain-rate sensitivity over the rate regime studied. Longer normalization times produce coarser carbide particles and lower flow stress levels. The stress level, however, does not change significantly with the increase in the normalization time from 48 to 120 hours (mean particle diameters 0.84–1.18 μm) whereas a significant reduction is seen between the 24 and 48 hour treatments (particle diameters from 0.54 to 0.84 μm).

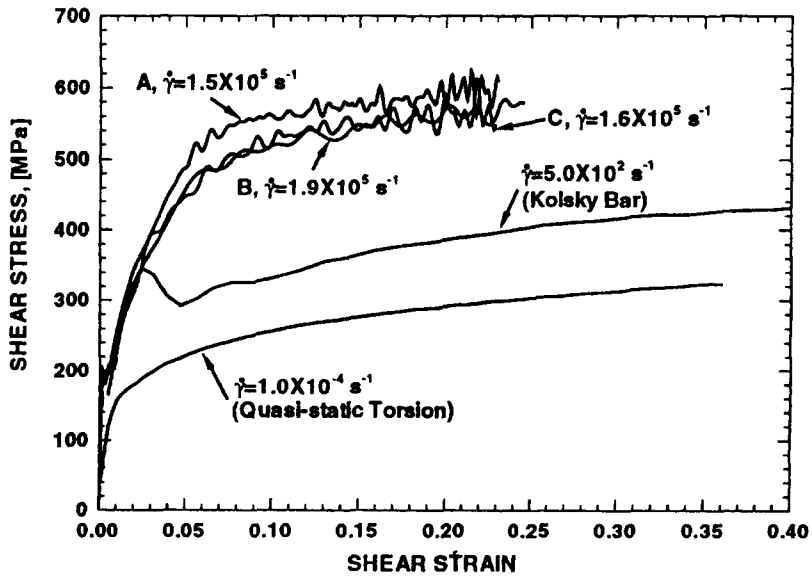

Fig. 2. Shear stress–strain curves of spheroidized 1045 steel obtained from pressure–shear plate impact, torsional Kolsky bar and quasistatic torsion.

The material response over the strain rate range from $10^{-4}\,s^{-1}$ to $1.5 \times 10^{5}\,s^{-1}$ is characterized by

$$\left.\begin{aligned} \dot{\bar{\varepsilon}} &= \frac{\dot{\varepsilon}_1 \dot{\varepsilon}_2}{\dot{\varepsilon}_1 + \dot{\varepsilon}_2}, \\ \dot{\varepsilon}_1 &= \dot{\varepsilon}_0 \left[\frac{\bar{\sigma}}{g(\bar{\varepsilon})}\right]^m, \\ \dot{\varepsilon}_2 &= \dot{\varepsilon}_m \exp\left[-\frac{ag(\bar{\varepsilon})}{\bar{\sigma}}\right], \\ g(\bar{\varepsilon}) &= \sigma_0[1 + \exp(\omega - \bar{\varepsilon}/\varepsilon_r)](1 + \bar{\varepsilon}/\varepsilon_0)^N, \end{aligned}\right\} \tag{2}$$

where $\bar{\varepsilon} = \int_0^t \dot{\bar{\varepsilon}}\,dt$ is the equivalent platic strain; $\dot{\varepsilon}_0$ is a reference strain rate; m and a are rate sensitivity parameters, respectively, for strain rates below $10^3\,s^{-1}$ and above $5 \times 10^4\,s^{-1}$; σ_0 is a reference stress; ε_0 is a reference strain; and N is the strain hardening exponent. The function $g(\bar{\varepsilon}, T)$ represents the stress–strain relation at a quasistatic strain rate of $\dot{\varepsilon}_0$.

Equation (2) provides a smooth transition between the measured response $\dot{\bar{\varepsilon}} = \dot{\varepsilon}_1(\bar{\sigma}, \bar{\varepsilon})$ at strain rates less than $10^3\,s^{-1}$, and the limiting behavior $\dot{\bar{\varepsilon}} = \dot{\varepsilon}_2(\bar{\sigma}, \bar{\varepsilon})$ at strain rates greater than say, $5 \times 10^4\,s^{-1}$. It also includes a limiting strain rate, $\dot{\varepsilon}_m$, which is not available from experiments, a value of $8 \times 10^8\,s^{-1}$ or greater is chosen, primarily for the numerical purpose of avoiding the need for unreasonably small time steps at early times when the strain rate and stresses are high. These stresses are relaxed in a few nanoseconds. The uncertainty in the response of the material at small strains and at shear strain rates greater than, say, $10^7\,s^{-1}$ is unvoidable at the present because of the lack of experimental data in this regime. This uncertainty may have an effect on the calculated initial impact response. However, this uncertainty in the initial response of the material is not expected to play a significant role in the ductile failure which occurs much later.

All the parameters are chosen to best fit the material response for specimens with normalization A, which are used in the subsequent dynamic ductile rupture experiments. Because the quasistatic curves and the torsional Kolsky bar curves were obtained from a spheroidized 1045 steel with a microstructure similar to that produced by normalization C which has a larger mean particle size and lower flow stress level, the parameters in the formulation are intentionally chosen to produce slightly higher flow stresses at the corresponding strain rates. It should be noted that pressure–shear plate impact experiments and torsional experiments provide more accurate measures of the material response at strains greater than a few percent than at very small strains. Parameters ω and ε_r are introduced to model the higher flow stress levels at small strains due to the lack of a large mobile dislocation density in the annealed material. These parameters are chosen by fitting the initial part of the velocity profiles at the rear surface from the normal impact experiment of unnotched specimens. Values of the parameters are listed in Table 3.

3. EXPERIMENT

The experimental configuration for the dynamic ductile rupture experiment is shown in Fig. 3. The specimen is a circular disk, 59 mm in diameter and 8 mm in thickness. The notch has a width of approximately 0.35 mm and is cut halfway through the diameter of the disk by electrical discharge machining (EDM). The notch is filled with stainless steel shims to transmit the compressive pulse. The experiment involved plane strain loading of the notched specimen by impacting it with a thin elastic flyer plate and reflecting the compressive pulse from the rear surface of the specimen. The flyer plate has a thickness of 3 mm and the same diameter as the specimen. The impact results in the loading of the specimen by a plastic wave whose main pulse has a duration of approximately one microsecond. Figure 4 shows the

Table 3. Material parameters

Spheroidized 1045 Steel (24 hour Normalization)
$\sqrt{3}\dot{\varepsilon}_0 = 1.0 \times 10^{-4}\,s^{-1}$, $m = 75$, $\varepsilon_0 = 310\,MPa$
$\sqrt{3}\dot{\varepsilon}_m = 5.0 \times 10^{8}\,s^{-1}$, $a = 15$
$\varepsilon_0 = 1.22 \times 10^{-5}$, $N = 0.13$
$\omega = 0.65$, $\varepsilon_r = 0.0043$
$\rho = 7850\,kg/m^3$
$E = 2.10 \times 10^{5}\,MPa$, $\nu = 0.29$
$\alpha = 1.0 \times 10^{-5}\,K^{-1}$

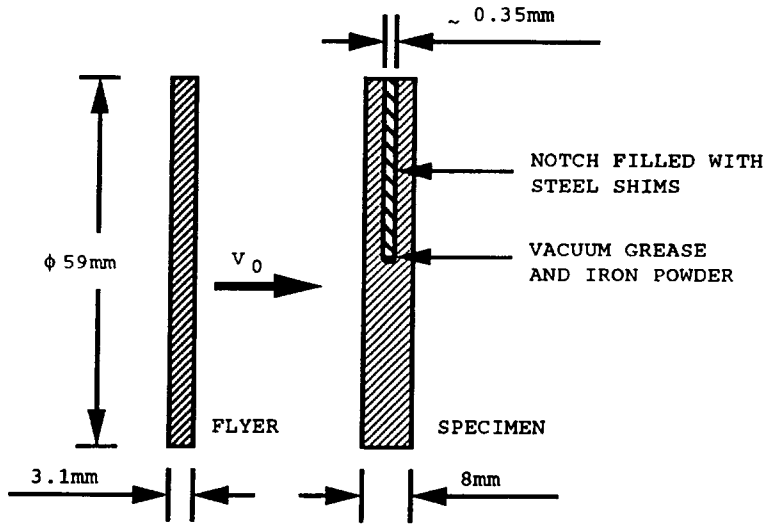

Fig. 3. Configuration of the dynamic ductile rupture experiment of a notched specimen.

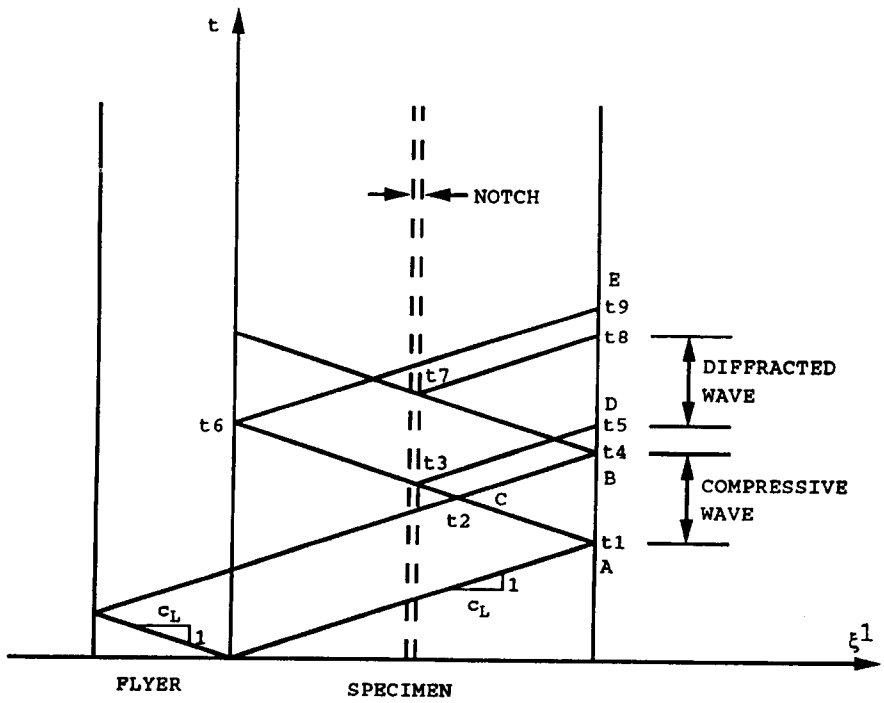

Fig. 4. Time-distance (Lagrangian) diagram for the dynamic ductile rupture experiment of a notched specimen.

time-distance diagram for the main wave fronts that traverse the specimen and flyer. Upon arrival at the notch (t_3) the reflected tensile wave is diffracted, causing straining at high rates around the notch tip. The reflected tensile wave and its diffraction by the notch causes dynamic ductile void nucleation, growth and coalescence in the specimen. To study the plastic wave profiles that propagate through the specimen and the ductile rupture (or spallation) caused by the tensile wave in the absence of the notch, one version of the experiment involves the impact of an unnotched specimen of the same dimensions. This type of tensile damage occurs near C in Fig. 4 where the stress first becomes tensile. These two types of experiments allow comparison of the ductile rupture processes initiated by a tensile plane plastic wave alone and by its diffraction from a blunt notch.

The motions at three separate points on the rear surface are monitored by a multi-beam velocity interferometer system shown in Fig. 5. By relating the motion of the rear surface at several points to the void nucleation and growth near the notch tip and to the occurrence of spallation, a better understanding can be obtained of the damage mechanisms under dynamic loading conditions. The multi-beamsplitting scheme used in the system has been described in detail by Mello *et al.* [39]. Each leg of the system is a normal velocity interferometer described by Barker [40]. A quadrature optical setup, similar to but different from those described by Hemsing [41] and Bouricius and Clifford [42], is used for one of the points (Fig. 5) to obtain two interference signals which are approximately 90° out of phase to allow unambiguous identification of the absolute phase of the interference signals.

4. NUMERICAL SIMULATION

Finite element simulation of the impact experiments is conducted by a finite deformation formulation by Needleman *et al.* [43–45]. The principal feature of this formulation that is of interest in the present investigation is the modeling of viscoplastic deformation and material failure due to the nucleation and growth of voids. The flow rule for a material containing voids is derived from a plastic potential introduced by Gurson [23,24] and modified by Tvergaard [25] and Tvergaard and Needleman [27]:

$$\Phi = \frac{\sigma_e^2}{\bar{\sigma}^2} + 2q_1 f^* \cosh\left(\frac{3q_2\sigma_h}{2\bar{\sigma}}\right) - 1 - q_1^2 f^{*2} = 0. \tag{3}$$

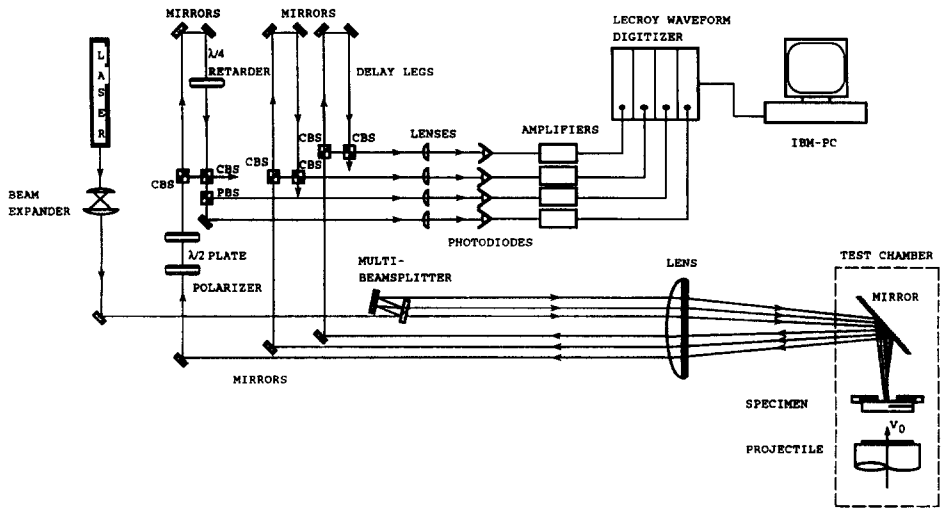

Fig. 5. Schematic of the setup of the dynamic ductile rupture experiment with a multi-beam velocity interferometer system.

In Eqn (3) σ_e and σ_h are the macroscopic equivalent Cauchy stress and the macroscopic hydrostatic stress, respectively, i.e.

$$\sigma_e^2 = \frac{3}{2}\boldsymbol{\sigma}':\boldsymbol{\sigma}'; \quad \sigma_h = \frac{1}{3}\boldsymbol{\sigma}:\mathbf{I}, \tag{4}$$

where $\boldsymbol{\sigma}$ and $\boldsymbol{\sigma}' = \boldsymbol{\sigma} - \sigma_h\mathbf{I}$ are the Cauchy and the deviatoric Cauchy stress tensors, respectively; $\mathbf{I}$ is the second order identity tensor and $\boldsymbol{\sigma}':\boldsymbol{\sigma}'$ denotes $\sigma'^{ij}\sigma'_{ji}$. The stress $\bar{\sigma}$ is an equivalent stress in the matrix material. Parameters q_1 and q_2 are dilatancy and pressure sensitivity parameters introduced by Tvergaard [25, 26]. The quantity f^* is a function of the void volume fraction f defined as

$$f^* = \begin{cases} f & f \le f_c; \\ f_c + \dfrac{f_u^* - f_c}{f_f - f_c}(f - f_c) & f \ge f_c, \end{cases} \tag{5}$$

where $f_u^* = 1/q_1$ is the value of f^* when the material loses all stress carrying capacity, corresponding to the rapid void coalescence in the final stages of ductile rupture; as $f \to f_f$, $f^* \to f_u^*$; f_c is the critical void volume fraction after which the material loses its strength at accelerated rates. Values for the parameters f_c, f_f, q_1, q_2 that are used in the simulation reported here are $f_c = 0.07$, $f_f = 0.15$, $q_1 = 1.25$, and $q_2 = 1.3$.

The plastic flow rule is obtained from (6.3) by writing the plastic part of the rate-of-deformation tensor, $\mathbf{D}^p$, as

$$\mathbf{D}^p = \dot{\Lambda}\frac{\partial \Phi}{\partial \sigma} = \dot{\Lambda}\left[\frac{3\boldsymbol{\sigma}'}{\bar{\sigma}^2} + 3q_1 q_2 f^* \sinh\left(\frac{3q_2\sigma_h}{2\bar{\sigma}}\right)\mathbf{I}\right], \tag{6}$$

where the proportionality factor $\dot{\Lambda}$ is obtained by equating plastic work rate to the matrix energy disspation rate.

Table 4. Experiments with unnotched specimens

Shot #	V_0 mm/μs	T_f mm	T_s mm	d mm
9006	0.155	3.12	8.12	2.34
9101	0.138	3.08	8.05	*
9102	0.141	3.08	8.01	**

*: no spall; **: void initiation observed in locations 2–2.4 mm from rear surface.

Table 5. Experiments with notched specimens

Shot #	V_0 mm/μs	W_0 mm	W mm	$\Delta W/W_0$ %	T_f mm	T_s mm	d mm
9002	0.140	0.372	0.438	17.6	3.06	7.98	*
9003	0.196	0.336	**	**	3.06	7.98	2.39
9004	0.150	0.343	0.521	52.0	3.18	8.05	2.22
9005	0.156	0.413	0.593	43.6	3.12	8.12	2.03

* No spall, void initiation observed; ** spall crack connected with notch; V_0: projectile velocity; W_0: average notch width before experiment; W: notch width at middle section after experiment; T_f: flyer thickness; T_s: specimen thickness; d: distance between spall plane and rear surface of specimen.

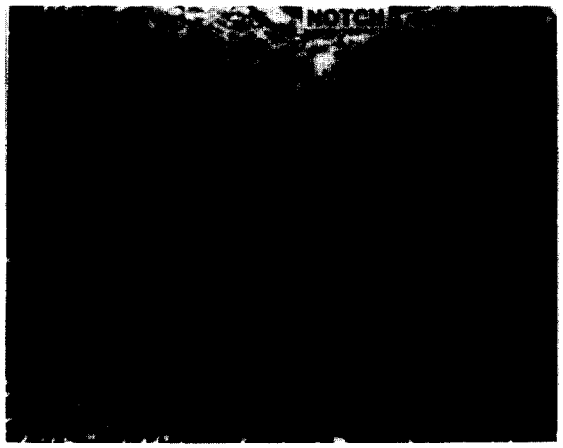

(a)

(b)

Fig. 6. Void nucleation in the notch tip region during Shot 9002, $V_0 = 0.140\,\text{mm}/\mu\text{s}$; (a) the notch tip region; and (b) a close-up view of the voids.

The damage parameter or the void volume fraction f evolves through the initiation of new voids and the growth of existing voids according to

$$\dot{f} = \dot{f}_{\text{nucleation}} + \dot{f}_{\text{growth}}. \tag{7}$$

In order to model void nucleation through both a strain-controlled mechanism and a stress-controlled mechanism the nucleation rate is taken to have the form

$$\dot{f}_{\text{nucleation}} = \mathscr{D}\dot{\bar{\varepsilon}} + \mathscr{B}(\dot{\bar{\sigma}} + \dot{\sigma}_h), \tag{8}$$

where

$$\mathscr{D} = \frac{f_N}{s_N\sqrt{2\pi}}\exp\left[-\frac{1}{2}\left(\frac{\bar{\varepsilon} - \bar{\varepsilon}_c - \varepsilon_N}{s_N}\right)^2\right], \tag{9}$$

$$\mathscr{B} = \frac{f_N}{\sigma_0 s_N\sqrt{2\pi}}\exp\left[-\frac{1}{2}\left(\frac{(\bar{\sigma} - \sigma_h) - \sigma_N}{\sigma_0 s_N}\right)^2\right]. \tag{10}$$

Parameter f_N is the volume fraction of void nucleating particles, σ_N is the mean void nucleation stress, s_N is the standard deviation of nucleation, $\bar{\varepsilon}_c$ is the accumulated equivalent

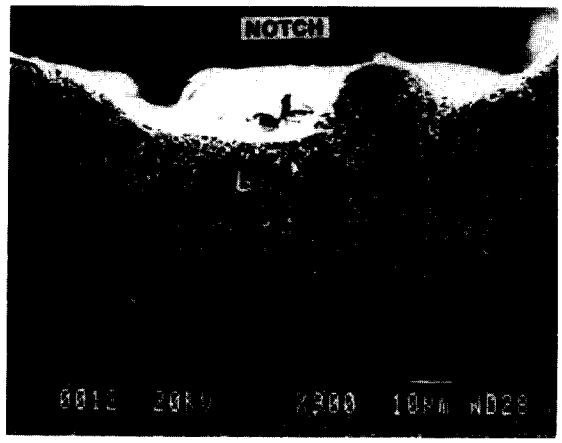

(a)

(b)

Fig. 7. Void nucleation, growth and coalescence in the notch tip region during Shot 9005, $V_0 = 0.156\,\text{mm}/\mu\text{s}$; (a) the notch tip region; and (b) a close-up view of the voids.

plastic strain during the initial compressive wave. It is assumed that plastic strain due to compressive loading does not contribute to the nucleation of voids. In the calculation, since initial deformation occurs under compression, the value of $\bar{\varepsilon}_c$ for a material element is taken as the total equivalent plastic strain at the time when the hydrostatic stress (σ_h) first becomes tensile there. The value of $\bar{\varepsilon}_c$ may be different for different locations of the specimen. The incorporation of $\bar{\varepsilon}_c$ in Eqn (9) eliminates the possibility of predicting void nucleation for plastic deformations under compressive loading. $\bar{\varepsilon}_c$ is not a model parameter and therefore is not listed in Table 3. Instead, it is calculated as the simulation progresses. Also, in Eqns (8–9), ε_N is the mean void nucleation strain and $\sigma_0 s_N$ is the standard deviation of stress-controlled nucleation. Values used for the respective parameters are: $f_N = 0.06\,\text{MPa}$, $s_N = 0.01$, and $\sigma_0 = 310\,\text{MPa}$. The growth rate of existing voids is determined from the plastic incompressibility of the matrix material as

$$\dot{f}_{\text{growth}} = (1-f)\mathbf{D}^p:\mathbf{I}. \tag{11}$$

The numerical implementation of the material model has been described by Needleman and Tvergaard [44, 45].

(a)

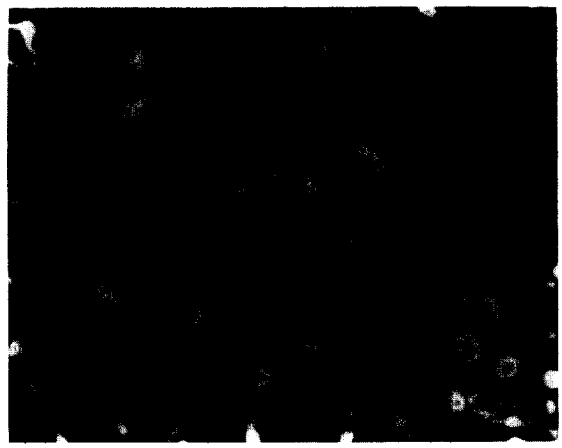

(b)

Fig. 8. Void growth and coalescence in the notch tip region during Shot 9005, $V_0 = 0.156\,\text{mm}/\mu\text{s}$; (a) the notch tip region showing a band of voids; and (b) a close-up view of the void band.

5. RESULTS AND DISCUSSION

Experiments conducted are summarized in Table 4 for the unnotched specimens and Table 5 for the notched specimens. All the experiments are conducted with flyers made of a Hampden high carbon tool steel which has a proportional limit of 1600 MPa in shear and remains elastic throughout the experiment.

The relative notch opening $\Delta W/W_0$ in Table 5 can be used as an approximate measure of the amount of plastic deformation that the notch tip material undergoes. The relative notch opening depends on the impact velocity as well as the initial notch width W_0. Smaller notch width corresponds to larger relative notch opening $\Delta W/W_0$ due to more intense tensile loading. When impact velocities are below $V_0 = 0.140\,\text{mm}/\mu\text{s}$, no significant void initiation was found. At impact velocities of approximately $V_0 = 0.140\,\text{mm}/\mu\text{s}$ the tensile wave reflected from the rear surface of the specimen begins to cause void nucleation at 2–2.4 mm from the rear surface. As the impact velocities are increased this tensile wave causes the material to fail. Scanning electron microscopic examination shows that the spallation initiates as cleavage of the ferrite matrix grains and is assisted by void coalescence as discussed in Section 5.1.

5.1. *Scanning electron microscopy*

The impacted specimens are sectioned along a plane perpendicular to the impact face and the notch front. The revealed surface is ground, polished, etched with 4% picral and examined in a JEOL 840F scanning electron microscope (SEM). Figures 6(a–b) show the notch tip region of the specimen from Shot 9002. Voids are found in a region within about 5–10 μm in front of the notch tip. Nucleation occurs through (a) particle–matrix debonding; (b) particle cracking; and (c) particle–particle separation as shown in Fig. 6(b). The voids show apparent growth after nucleation. The notch width, which was approximately 372 μm wide initially, increased by 17.6% to 438 μm after the impact. As the impact velocity is increased to 0.156 mm/μs (Shot 9005) voids are found in a larger region, approximately 30–40 μm in front of the notch tip (Fig. 7). The voids show substantial growth, and begin to coalesce, as shown in Figs 7(a–b). This is the result of the increased amount of plastic straining as indicated by the relative notch width increase of 43.6% at this impact velocity. The growth and coalescence of voids lead to the onset of ductile rupture at the immediate notch tip region where severe plastic straining occurs, as shown in Fig. 7. Figures 8(a–b) show that void growth tends to localize in areas at the notch tip region. These areas often appear as bands extending from the notch tip where a cavity is formed. The voids inside the bands undergo substantial growth and coalescence. The formation of these void bands may be related to notch surface defects existing before the experiments.

Voids also appear in a strip about 2–2.4 mm from the rear surface in the unnotched lower half of the specimen. These are initiated by the reflected tensile wave. The voids in the strip do not show substantial growth at impact velocities on the order of $V_0 = 0.140$ mm/μs. As the impact velocity is increased the material ruptures along a plane parallel to the rear surface. Figure 9 is a schematic which summaries the locations of the material damages in a notched

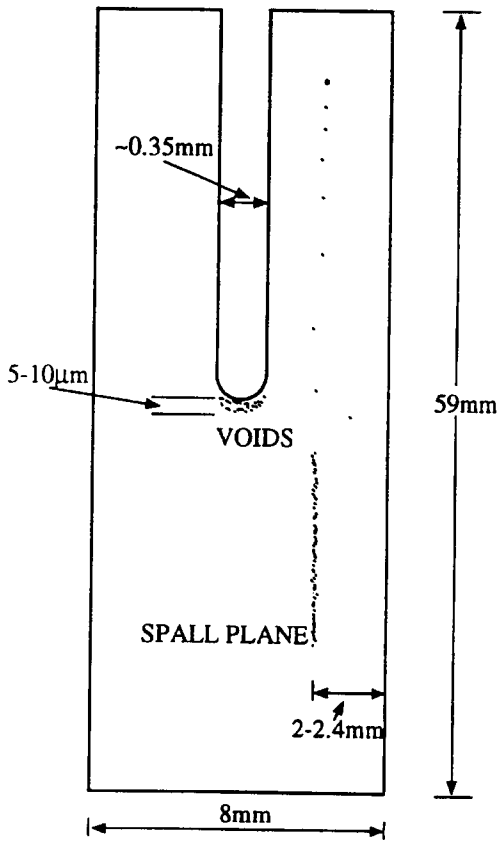

Fig. 9. Schematic of damages mechanisms in dynamic ductile rupture experiment of a notched specimen.

specimen during the experiments. Clearly, damage occurs by void nucleation, growth and coalescence in the notch tip region and by spallation along a plane parallel to the rear surface of the specimen. Impact experiments of unnotched specimens as well as notched specimens show that when the tensile wave is not sufficient to spall the specimen, voids can initiate during the tensile pulse, but they are relatively small. Spallation results if the impact velocity is increased to a value higher than 0.150 mm/μs. Figures 10(a–b) show the typical morphology of the spalled regions (Shot 9005). Only a few voids are observed along the spall plane. It appears that spallation initiates as cleavage fracture fragments. These segments link by lateral shear, which involves void growth and coalescence. This observation is supported by a study of the spall plane (Fig. 11) which shows transgranular cleavage of the ferrite matrix and cleavage facets connected by ductile necking of the matrix material. The transgranular cleavage planes link up via inclined void sheets which are formed through the lateral shear seen in Fig. 10. These void sheets appear to form primarily at grain boundaries [Fig. 11(a)]. Also in Fig. 11(a) cementite particles are distributed on the cleaved surfaces, suggesting that the particles play a role in the formation of the cleavage planes. Small necks are seen on facets of the cleaved surfaces, indicating a combination of ductile deformation and failure by cleavage of the ferrite matrix.

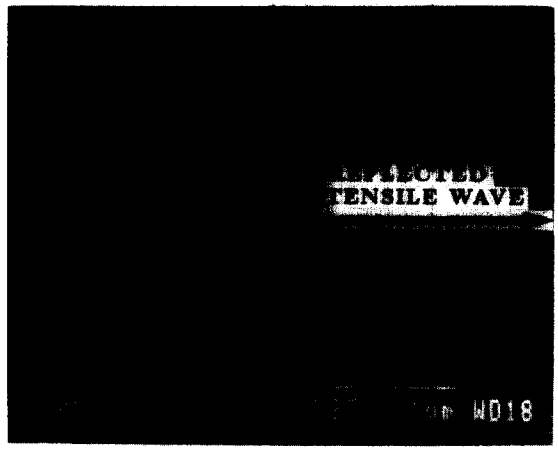

(a)

(b)

Fig. 10. Spalled plane formed due to the reflected tensile wave after Shot 9005, $V_0 = 0.156$ mm/μs; (a) an overview of the spall plane, and (b) linkage of segments of the spall plane through lateral shear.

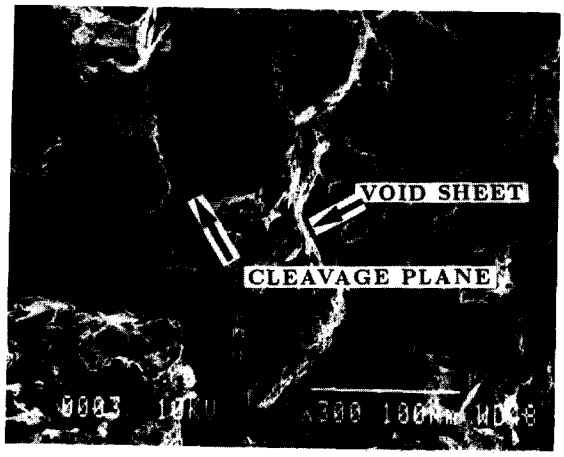

(a)

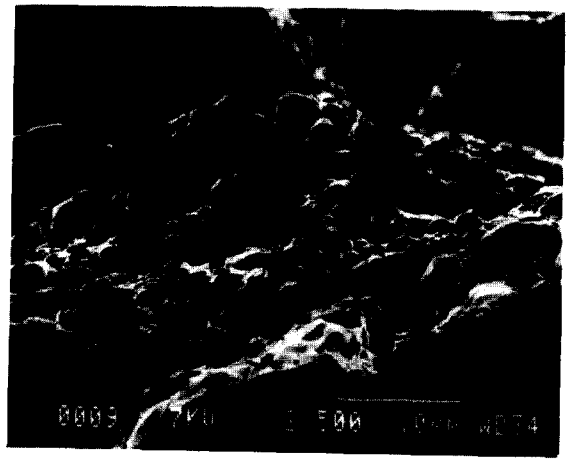

(b)

Fig. 11. Fractograph of the spall plane surface after Shot 9006 of the unnotched specimen, $V_0 = 0.155\,\text{mm}/\mu\text{s}$; (a) spall plane surface showing void sheets and cleaved planes, and (b) a close-up view of a void sheet.

The void band is observed only on the unnotched half of the specimen. A small number of nucleating voids are observed at the same distance from the rear surface on the notched half. The explanation may be that the tensile wave is reflected back toward the rear surface by the notch surface as a compressive wave, thereby reducing the duration of the tensile loading and keeping the putative spall plane in compression for most of the loading time.

5.2. *Free surface velocity–time profiles*

Figure 12 shows the free surface velocity profiles from the experiments with unnotched specimens listed in Table 3. The parts of the profiles corresponding to the different wave fronts shown in the distance-time diagram (Fig. 4) are labeled as: A—Arrival of the compressive wave at the rear surface; B—unloading of the main compressive pulse at the rear surface; C—tensile damage location (Fig. 4) and its arrival at the rear surface (Fig. 12); D—damage signal at the rear surface; and E—reflected compressive pulse arriving at the rear surface. The initial part of the experimental curves is used to determine the material parameters ω and γ_r in (2). These two parameters are introduced to model the higher flow stresses at small strains due to the lack of a large mobile dislocation population in the annealed material.

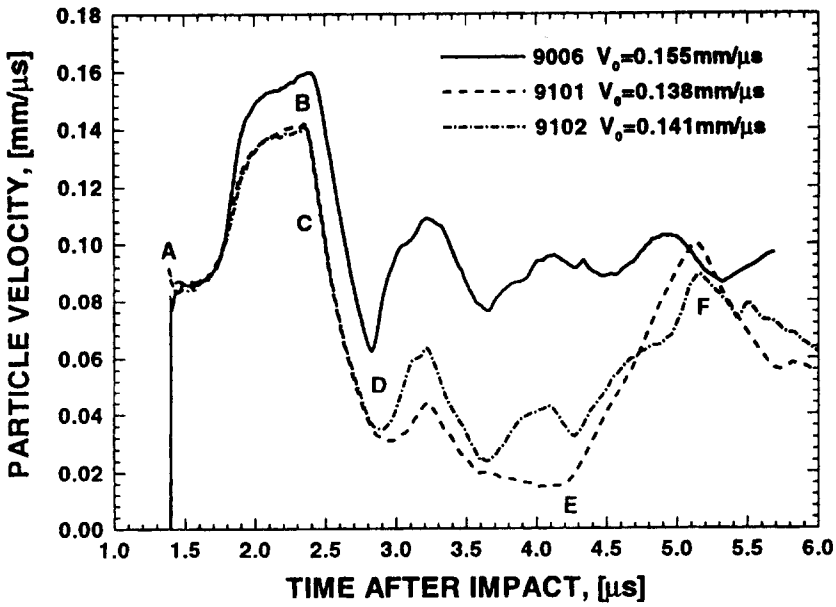

Fig. 12. Free surface particle velocity profiles for the unnotched specimen, Shot 9006 ($V_0 = 0.155$ mm/μs), 9101 ($V_0 = 0.141$ mm/μs), and 9102 ($V_0 = 0.138$ mm/μs).

The calculated profiles are shown in Fig. 13 for an impact velocity of $V_0 = 0.140$ mm/μs. Curve A represents the case without void nucleation and growth. Curves B and C correspond to cases with the nucleation strain $\varepsilon_N = 0.042$ and $\varepsilon_N = 0.041$, respectively, without stress-activated nucleation. Clearly, the "bumps" (which is due to the partial reflection of the tensile wave from a damaged material cross section) at about 2.9 μs correlate with a damage mechanism through the nucleation and growth of voids. Reducing the nucleation strain increases the amount of damage as indicated by the height of the "bumps". This damage corresponds to voids located approximately 2.0–2.4 mm from the rear surface. This interpretation is confirmed by the SEM observation described above. Void nucleation occurs at these locations for impact velocities in the order of 0.140 mm/μs and that spallation occurs at

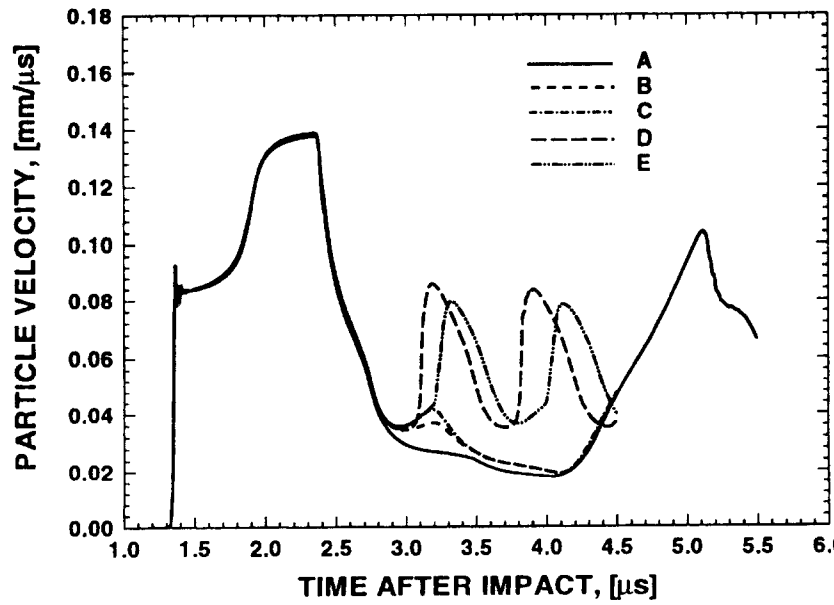

Fig. 13. Calculated free surface particle velocity profiles for the unnotched specimen, $V_0 = 0.140$ mm/μs.

higher impact velocities through transgranular cleavage and ductile reupture by void growth and coalescence. The effect of stress-controlled nucleation described by Eqn (10) is shown by curves D and E. These two curves correspond to the same cases represented by curves B and C, respectively, but with the stress-controlled nucleation activated. The nucleation stress $\sigma_N = 2550$ MPa for curve D and $\sigma_N = 2650$ MPa for curve E. The curves clearly show that decreasing the nucleation stress enables the tensile damage to occur earlier. The sinusoidal velocity profiles indicate that a spall plane has formed, as observed in the experiments. A pulse of the stress wave is trapped in the part of the specimen between the spall plane and

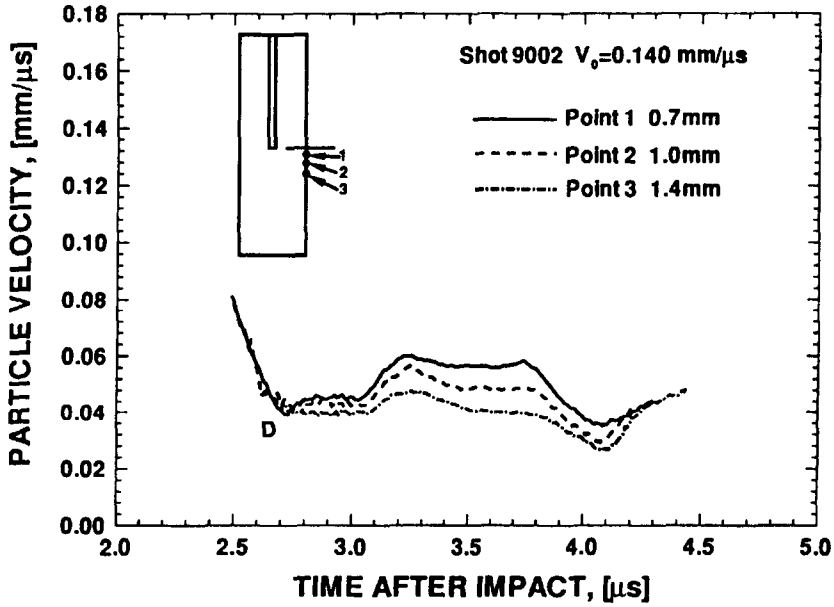

Fig. 14. Free surface particle velocity profiles at three points for the notched specimen, Shot 9002 ($V_0 = 0.140$ mm/μs). Distances from the notch tip: point 1–0.7 mm, point 2–1.0 mm, and point 3–1.4 mm.

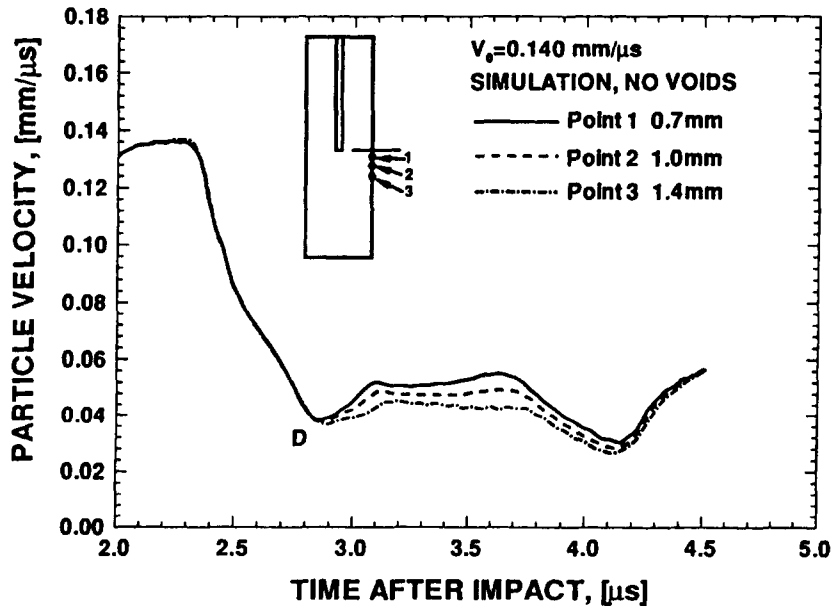

Fig. 15. Calculated free surface particle velocity profiles at three points for the notched specimen, ($V_0 = 0.140$ mm/μs). Distances from the notch tip: point 1–0.7 mm, point 2–1.0 mm, and point 3–1.4 mm.

the rear surface. This pulse reverberates in this part of the specimen and causes the rear surface velocity to oscillate.

Figure 14 shows the free surface velocities at three points, located at 0.7 mm, 1.0 mm and 1.4 mm in front of the notch tip, for Shot 9002. Only the time interval after the arrival of the main compressive wave is shown. Point D corresponds to the arrival of the diffracted wave at the rear surface. This cylindrical wave is generated by the tensile wave upon impingement on the notch tip. Figure 15 shows the corresponding calculated velocity profiles with void nucleation and growth in the model suppressed. The computed profiles represent velocity profiles without damage. The calculated profiles coincide with the experimetnal profiles, except for slightly higher levels of velocities. Therefore, in this particular experiment shown (Shot 9002), the nucleation and growth of voids do not appear to significantly influence the velocity profiles at the points measured.

6. CONCLUDING REMARKS

An impact configuration to study dynamic ductile rupture is presented. The experiments use both notched and unnotched specimens. Ductile void nucleation and growth occur due to the reflected tensile wave alone and to its diffraction from a blunt notch. Void growth is observed in the notch tip area when impact velocity reaches 0.140 mm/μs. Void coalescence occurred with increased plastic straining and higher stresses at high impact velocity. As the impact velocity is increased above 0.150 mm/μs, tensile wave induced spall occurs independently of the presence of a notch in the specimen. The spallation appears to be a combination of ductile void nucleation, growth, coalescence and transgranular cleavage of ferrite matrix assisted by cementite particles.

Numerical similations of the impact experiments have produced free surface velocity profiles that identify the damage signals observed in the rear surface velocity profiles with the void nucleation, growth and coalescence and spallation in the specimen. For the unnotched specimen, the calculated profiles agree with the measured profiles. For the notched specimen, compared with the results involving unnotched specimens, the rear surface velocity profiles for notched specimens are less sensitive to the nucleation, growth and coalescence of the voids in the notch tip region under the conditions studied.

Acknowledgments—This research is supported by the Army Research Office. Computations described here were carried out on a CRAY Y-MP8/864 at the San Diego Supercomputer Center. We would like to thank Professor A. Needleman of Brown University for his assistance in the finite element simulations.

REFERENCES

1. Dew-Hughes, D. and Robertson, W. D., Dispersed particle hardening of aluminum–copper alloy single crystals. *Acta Metallica*, 1960, Vol. 8, March, 147–155.
2. Meiklejohn, W. H. and Skoda, R. E., Dispersion hardening. *Acta Metallica*, 1960, Vol. 8, 773–780.
3. Ashby, M., The hardening of metals by non-deforming particles. *Z. Metallk.*, 1964, **55**, 5–17.
4. Kocks, U. F., A statistical theory of flow stress and work-hardening. *Phil. Mag.*, 1966, **13**, 541–566.
5. Foreman, A. J. E. and Makin, J. M., Dislocation movement through random arrays of obstacles. *Phil. Mag.*, 1966, **13**, 911–924.
6. Liu, C. T. and Gurland, J., The strengthening mechanism in spheroidized carbon steels. *Transactions of Metall. Soc. AIME*, 1968, **242**, 1535–1542.
7. Gurland, J. and Plateau, J., The mechanism of ductile rupture of metals containing inclusions. *Transactions of ASM*, 1963, **56**, 442–456.
8. Thomson, R. D. and Hancock, J. W., Ductile failure by void nucleation, growth and coalescence. *International Journal of Fracture*, 1984, **26**, 99–112.
9. Thompson, A. W., Modeling of local strains in ductile fracture. *Metall. Trans. A*, 1987, **18A**, 1877–1886.
10. McClintock, F. A., A criteria for ductile fracture by the growth of holes. *Journal of Applied Mechanics*, 1968, **35**, 363–371.
11. Rice, J. R. and Tracey, D. M., On the ductile enlargement of voids in triaxial stress fields. *Journal of Mechanics and Physics of Solids*, 1969, **17**, 201–217.
12. Brownrigg, A., Spitzig, W. A., Richmond, O., Teirlinck, D. and Embury, J. D., The influence of hydrostatic pressure on the flow stress and ductility of a spheroidized 1045 steel. *Acta Metallica*, 1983, **31**(8), 1141–1150.

13. Broek, D., The role of inclusions in ductile fracture and fracture toughness. *Engngineering Fracture Mechanics*, 1973, **5**, 55–66.
14. In-Gyu Park and Thompson, A. W., Ductile fracture in spheroidized 1520 steel. *Acta Metallica*, 1988, **36**(7), 1653–1664.
15. Fisher, J. R. and Gurland, J., Void nucleation in spheroidized carbon steels, parts I and II. *Metal Science*, 1981, May, 185–202.
16. Berg, C. A., The motion of cracks in plane viscous deformation. *Proceedings of the 4th U.S. National Congress on Applied Mechanics*. 1962 Vol. 2, 885–892.
17. Budiansky, B., Hutchinson, J. W. and Slutsky, S., Void growth and collapse in viscous solids. In *Mechanics of Solids, The Rodney Hill 60th Anniversary Volume*, eds H. G. Hopkins and M. J. Sewell, Pergamon, Oxford 1982, pp. 13–45.
18. Budiansky, B., Micromechanics. *Computers and Structures*, 1983, **16**, 3–12.
19. Thomason, P. F., A theory for ductile fracture by internal necking of cavities. *Journal of the Institute of Metals*, 1968, **96**, 360–365.
20. Blume, J. A., The finite deformation and stress fields near a pair of spherical cavities in nonlinearly elastic solids. *Proceedings of the Symposium on Three-dimensional Fracture Processes*. Berkeley, CA, June, 1988.
21. Nemat-Nasser, S. and Iwakuma, T., NASA Conference Publication No. 2271, 113, 1982.
22. Nemat-Nasser, S., Iwakuma, T. and Accorsi, M., Cavity growth and grain boundary sliding in polycrystalline solids. *Mechanics of Materials*, 1986, **5**, 317–329.
23. Gurson, A. L., Plastic flow and fracture behavior of ductile materials incorporating void nucleation, growth and interaction. Ph.D. Thesis, Brown University, Providence, RI,1975.
24. Gurson, A. L., Continuum theory of ductile rupture by void nucleation and growth - I. Yield criteria and flow rules for porous ductile materials. *Journal of Engineering Mat. Tech.*, 1977, **99**, 2–15.
25. Tvergaard, V., Influence of voids on shear band instabilities under plane strain conditions. *International Journal of Fracture*, 1981, **17**, 389–407.
26. Tvergaard, V., On localization in ductile materials containing spherical voids. *International Journal of Fracture.*, 1982, **18**, 237–252.
27. Tvergaard, V. and Needleman, A., Analysis of the cup-cone fracture in a round tensile bar. *Acta Metallica*, 1984, **32**, 157–169.
28. Nemat-Nasser, S. and Hori, M., Void collapse and void growth in crystalline solids. *Journal of Applied Physics*, 1987, **62**, 2746–2755.
29. Hori, M. and Nemat-Nasser, S., Mechanics of void growth and void collapse in crystals. *Mechanics of Materials*, 1988, **7**, 1–13.
30. Hori, M. and Nemat-Nasser, S., Dynamic response of crystalline solids with microcavities. *Journal of Applied Physics*, 1988, **64**, 856–863.
31. Curran, D. R. and Seaman, L., Dynamic failure of solids. *Physics Reports*, 1983, **147** (5–6), 255–388.
32. Meyers, M. A. and Aimone, C. T., Dynamic fracture (spalling) of metals. *Progress in Material Science*, 1983, **28**, 1–96.
33. Asay, J. R. and Kerley, G. I., The response of materials to dynamic loading. *International Journal of Impact Engineering*, 1987, **5**, 69–99.
34. Rajendran, A. M., A void growth based failure model to describe spallation. *Dynamic Constitutive/Failure Models*. eds A. M. Rajendran and T. Nicholas, Dayton, OH, May 1988, pp. 111–144.
35. Eftis, J., Nemes, J. A. and Randles, P. W., Viscoplastic analysis of plate-impact spallation. *International Journal of Plasticity*, 1991, **7**, 15–39.
36. Underwood, E. E., *Quantitative Stereology*. Addison-Wesley, 1970.
37. Clifton, R. J. and Klopp, R. W., Pressure–shear plate impact testing. *Metals Handbook*, Vol. 8, Amer. Soc. Metals, Metals Park, 9th ed., 1985, pp. 230–239.
38. Walter, M. and Duffy, J., Brown University Thesis, Brown University, Providence, RI, 1990.
39. Mello, M. C., Prakash, V. and Clifton, R. J., Multi-point interferometer for monitoring two dimensional wave motions. *APS Topical Conference on Shock Compression of Condensed Matter*, 17–20 June 1991, Williamsburg, VA.
40. Barker, L. M., *Behavior of Dense Media Under High Dynamic Pressures*. Gordon and Breach, NY, 1968, p. 483.
41. Hemsing, W. F., Velocity sensing interferometer (VISAR) modification. *Review of Scientific Instruments*, 1979, **50**(1), 73–77.
42. Bouricius, G. M. B. and Clifford, S. F., An optical interferometer using polarization coding to obtain quadrature phase components. *Review of Scientific Instruments*, 1970, **41**(12), 1800–1803.
43. Tvergaard, V. and Needleman, A., An analysis of temperature and rate dependence of charpy v-notch energies for a high nitrogen steel. *International Journal of Fracture*, 1988, **37**, 197–215.
44. Needleman, A. and Tvergaard, V., An analysis of dynamic, ductile crack growth in a double edge cracked specimen. *International Journal of Fracture*, 1991,**49** (1), 41–67.
45. Needleman, A. and Tvergaard, V., Numerical study of void distribution effects on dynamic, ductile crack growth. *International Journal of Fracture*, 1991, **38** (2–3), 157–173.